Vol. 47 (2016) *ACTA PHYSICA POLONICA B* No 6

STANDARD MODEL RESULTS FROM ATLAS — EARLY 13 TeV DATA*

JANUSZ CHWASTOWSKI

on behalf of the ATLAS Collaboration

The Henryk Niewodniczański Institute of Nuclear Physics
Polish Academy of Sciences
Radzikowskiego 152, 31-342 Kraków, Poland

(Received April 7, 2016)

Selected Standard Model measurements obtained with the ATLAS detector at the LHC using the early 13 TeV data are presented.

DOI:10.5506/APhysPolB.47.1417

1. Introduction

During the Long Shutdown 1 (LS1), the LHC underwent several improvements. In consequence, it delivers proton beams accelerated to 6 500 GeV. In August 2015, the machine bunch time spacing was changed from 50 ns to 25 ns. In September, the LHC beam emittance was improved which resulted in a rapid growth of the delivered luminosity.

During the LS1, the ATLAS detector [1] was upgraded and refurbished. The detector upgrade and performance were discussed by M. Wessels and H. Ma during this conference. The detector parts, important for the analyses presented below, were:

- a new layer of a silicon pixel detector, the so-called Insertable B Layer (IBL), located next to the new beam pipe;
- refurbished Minimum Bias Trigger Scintillators (MBTS) wheels whose construction was slightly changed and which cover a slightly larger pseudorapidity[1] range as compared to the previous set-up.

---

* Presented at the Cracow Epiphany Conference on the Physics in LHC Run 2, Kraków, Poland, January 7–9, 2016.

[1] The pseudorapidity is defined as $\eta = -\log\tan\theta/2$, where θ is the polar angle.

The data presented below were taken at an early stage of the LHC Run 2. These data were taken with different values of the average number of proton–proton interactions per bunch crossing, $\langle\mu\rangle$. In 2015, the ATLAS detector reached the efficiency of data taking of about 90%.

2. Charged particle spectra

Charged particle spectra are basic distributions to be measured. Their measurement is discussed at length in [2]. The data presented below were collected during the low instantaneous luminosity runs with the average number of pp interactions per bunch crossing, $\mu = 0.005$. The sample contains about 9 000 000 events triggered using the minimum bias trigger. The events were required to contain a single vertex and at least one charged particle. The distributions were constructed using good quality tracks registered within the $|\eta| < 2.5$ region and having the transverse momentum $p_{\mathrm{T}} > 0.5$ GeV. Only stable charged particles were considered *i.e.* those produced in pp interactions characterised by the lifetime $\tau > 300$ ps or the charged decay products of particles with $\tau < 30$ ps. Contrary to earlier analyses, strange baryons were excluded from the stable charged particles definition. The η, p_{T}, charged-particle multiplicity, n_{ch} and $\langle p_{\mathrm{T}}\rangle$ *vs.* n_{ch} distributions were measured. The results were corrected for experimental effects and unfolded to the particle-level (see [2] for details). The predictions of the Monte Carlo models, listed in Table I, were compared to the experimental data.

TABLE I

Monte Carlo generators used to generate the prediction.

Generator	Ver.	PDF	Tune	Focus
PYTHIA 8 [3]	8.186	MSTW2008LO [4]	A2 [5]	MB
PYTHIA 8	8.186	NNPDF2.3LO [6]	Monash [7]	MB/UE
EPOS [8]	LHCv3400	N/A	LHC	MB
QGSJET [9]	II-04	N/A	Default	MB

Figure 1 shows the multiplicity (left) and the transverse momentum (right) distributions together with various Monte Carlo predictions. The largest uncertainties are coming from tracking. As can be observed, EPOS provides a good description of the central plateau of the η distributions, however, it does not reproduce the forward regions. PYTHIA 8 A2 underestimates the plateau height by about 3%. QGSJET II-04 and PYTHIA 8 Monash overshoot the data by about 15% and 5%, respectively. A similar picture is seen in the case of p_{T} distribution — see Fig. 1 (right). Again, EPOS provides a good description. Both tunes of PYTHIA reasonably describe the data for lower values of p_T but over predict the spectrum for high p_T values. QGSJET II-04 predictions do not reproduce the data.

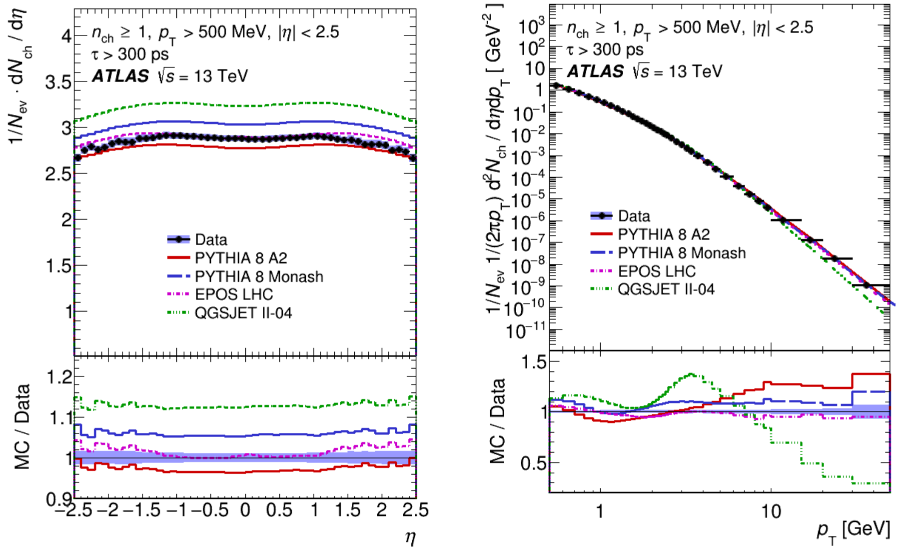

Fig. 1. Left: pseudorapidity distribution of charged particles within the $|\eta| < 2.5$ region. Right: the transverse momentum distribution of charged particles within the $|\eta| < 2.5$ region. From [2].

Figure 2 (left) shows the charged-particle multiplicity distribution. Also predictions of Monte Carlo models are depicted in the figure. PYTHIA 8 A2, a minimum bias tune, provides a proper description of the data up to $n_{ch} \approx 50$, while PYTHIA 8 Monash, EPOS, QGSJET II-04 reasonably describe the charged-particle multiplicity distribution in the region limited by $n_{ch} \approx 30$.

The dependence of $\langle p_T \rangle$ on the charged-particle multiplicity is presented in Fig. 2 (right) together with predictions of the models. EPOS gives a good description of the measured dependence. Both PYTHIA 8 A2 and Monash predict faster increase of $\langle p_T \rangle$ with increasing n_{ch} than measured. The QGSJET II-04 model fails to describe the data predicting basically a flat dependence.

The increase of $\langle p_T \rangle$ with increasing n_{ch} is a colour coherence effect. Assuming that the multiparton interactions dominate high multiplicity events and that there is an absence of colour coherence effects, the $\langle p_T \rangle$ should be approximately independent of n_{ch}. However, if the colour reconnection effects are present, then the charged-particle multiplicity decreases for a given number of multiparton interactions and hence the p_T per track increases.

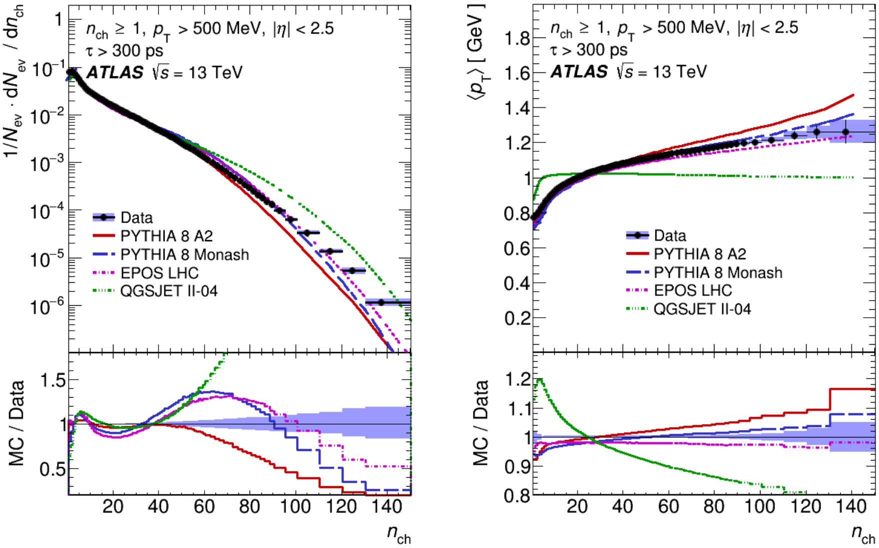

Fig. 2. Left: the multiplicity distribution of charged particles within the $|\eta| < 2.5$ region. Right: the $\langle p_{\mathrm{T}} \rangle$ *vs.* n_{ch} dependence for charged particles within the $|\eta| < 2.5$ region. From [2].

Figure 3 shows the centre-of-mass energy dependence of the charged-particle multiplicity within the $|\eta| < 0.2$ interval. To compare the present and lower energy measurements, the strange baryon contribution was added. The value of the correction is $\Delta_{\mathrm{ch}} = 1.015 \pm 0.009$.

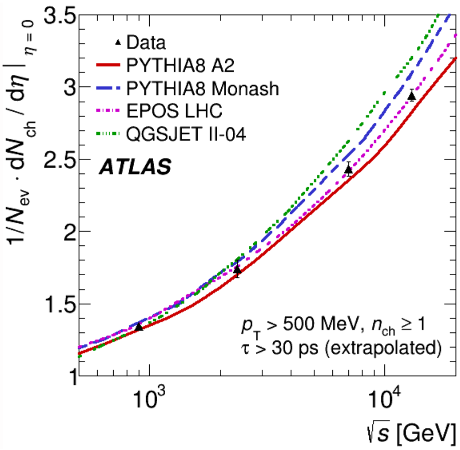

Fig. 3. The multiplicity of charged particles with $|\eta| < 0.2$ as a function of $\sqrt{s}$. The data were corrected for strange baryon contribution. From [2].

One can observe an increase by a factor of about 2.2 (about 1.2) between 900 GeV (8 TeV) and 13 TeV. The data follow the trend observed at lower energies. The data are well-described by EPOS and PYTHIA 8 A2 predictions, while PYTHIA 8 Monash and QGSJET-II overestimate the measured dependence.

3. Underlying event

Underlying event (UE) is the activity accompanying any hard scattering in a collision event. The beam remnants, multiparton interactions as well as the initial- and final-state radiation contribute to the underlying event. The UE activity cannot be uniquely separated from the hard process on the event-by-event basis. The underlying event activity is studied using the following observation. The influence of the hard process should be minimised in the plane perpendicular to its axis. Therefore, one selects a leading particle of a given p_{T} and divides the event into regions in the azimuthal angle calculated w.r.t. the leading particle $\vec{p}_{\mathrm{T}}$ as shown in Fig. 4.

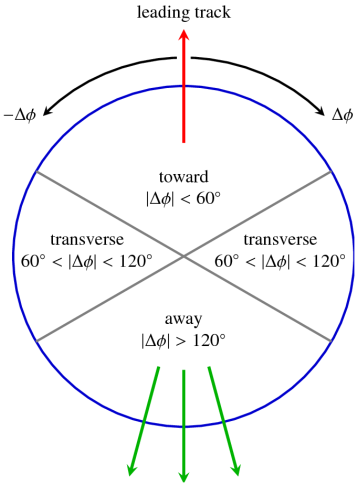

Fig. 4. The azimuthal regions used in the underlying event studies. From [10].

The interval containing the leading particle is called the *toward* region, the one opposite to it is the *away* region. The UE activity is studied in the *transverse* region with the *toward* and *away* regions treated as the control ones. The analysis was performed using the same data as for the charged particle spectra measurements. It has to be stressed that the underlying event activity was investigated using *the detector level information* to which the predictions of the Monte Carlo models are compared — see [10] for full details.

Typically, one studies the distributions of the scalar sum of particle transverse momenta, Σp_{T}, and of the charged particle multiplicity, N_{ch}, in the defined angular regions or these distributions as a function of the leading particle p_{T}. In the angular regions, one expects to observe a gradual transition from the minimum bias type distributions to the hard process ones with increasing value of the leading particle transverse momentum, $p_{\mathrm{T}}^{\mathrm{lead}}$. Indeed, such a behaviour can be observed in Figs. 5 (left) and 5 (right) showing $\langle \mathrm{d}^2\Sigma p_{\mathrm{T}}/\mathrm{d}\eta \mathrm{d}|\Delta\phi|\rangle$ and $\langle \mathrm{d}^2 N_{\mathrm{ch}}/\mathrm{d}\eta \mathrm{d}|\Delta\phi|\rangle$ distributions, respectively.

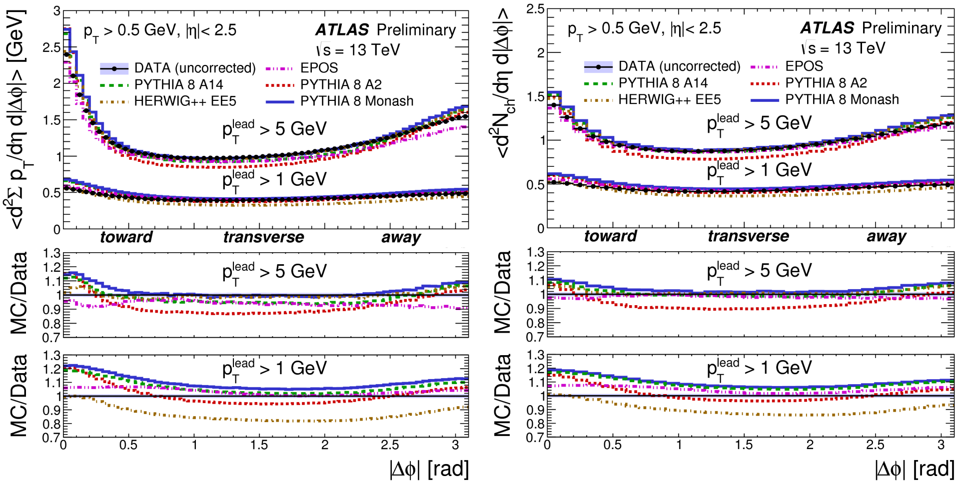

Fig. 5. Left: $\langle \mathrm{d}^2\Sigma p_{\mathrm{T}}/\mathrm{d}\eta \mathrm{d}|\Delta\phi|\rangle$ for charged particles. Right: $\langle \mathrm{d}^2 N_{\mathrm{ch}}/\mathrm{d}\eta \mathrm{d}|\Delta\phi|\rangle$ in different azimuthal angle regions. Predictions of various Monte Carlo models are also shown. From [10].

One can observe a gradual transition from the minimum bias to the hard event structure. Both distributions show a developing structure in the toward and away regions with increasing value of $p_{\mathrm{T}}^{\mathrm{lead}}$. It may be related to the increasing importance of the jet-like configurations. PYTHIA 8 A2 and EPOS provide a better description of the distributions measured for $p_{\mathrm{T}}^{\mathrm{lead}} > 1$ GeV. These two models were tuned using the minimum bias data gathered at $\sqrt{s} = 8$ TeV. The underlying event Monte Carlo tunes: PYTHIA 8 A14 [11] and PYTHIA 8 Monash give predictions which are closer to the distributions measured for $p_{\mathrm{T}}^{\mathrm{lead}} > 5$ GeV.

The $\langle \mathrm{d}^2\Sigma p_{\mathrm{T}}/\mathrm{d}\eta \mathrm{d}\phi\rangle$ and $\langle \mathrm{d}^2 N_{\mathrm{ch}}/\mathrm{d}\eta \mathrm{d}\phi\rangle$ distributions as the functions of $p_{\mathrm{T}}^{\mathrm{lead}}$ in the transverse region of the azimuthal angle are shown in Fig. 6. Both observables show a similar behaviour. There is an initial rise and then the distribution flattens off. In the case of $\langle \mathrm{d}^2 N_{\mathrm{ch}}/\mathrm{d}\eta \mathrm{d}\phi\rangle$ distribution, an approximate plateau for $p_{\mathrm{T}}^{\mathrm{lead}} > 6$ GeV can be observed. None of the Monte Carlo models delivers a proper description of the initial rise. Both

PYTHIA tunes, A2 and A14, as well as Herwig++ UE-EE5 [12] are closer to the data for $p_{\mathrm{T}}^{\mathrm{lead}} > 8$ GeV. EPOS fails to describe the presented distributions for $p_{\mathrm{T}}^{\mathrm{lead}} > 6$ GeV, which is the consequence of the absence of semi-hard minimum bias processes in the model.

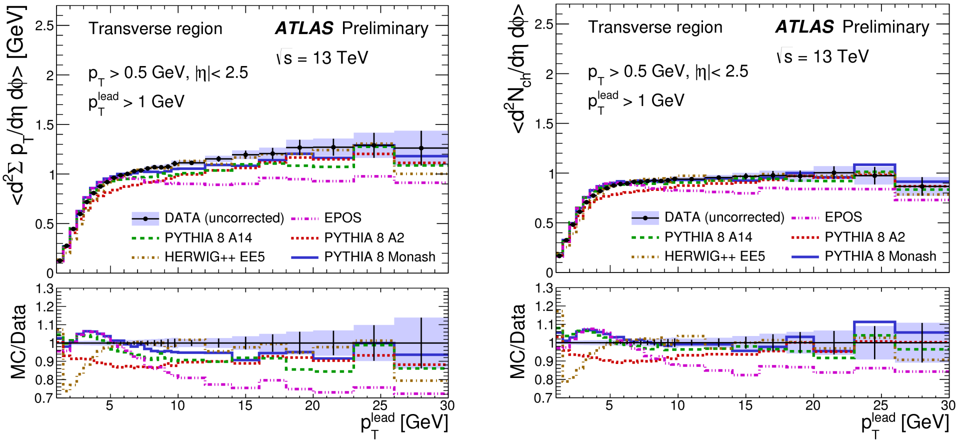

Fig. 6. Left: $\langle \mathrm{d}^2 \Sigma p_{\mathrm{T}}/\mathrm{d}\eta\mathrm{d}\phi\rangle$ for charged particles. Right: $\langle \mathrm{d}^2 N_{\mathrm{ch}}/\mathrm{d}\eta\mathrm{d}\phi\rangle$ as a function of $p_{\mathrm{T}}^{\mathrm{lead}}$ in the transverse azimuthal angle region. Predictions of various Monte Carlo models are also presented. From [10].

4. Inelastic cross section

The inelastic cross-section measurement is one of the basic measurements to be performed at every newly accessible energy. Since this observable belongs to the non-perturbative QCD domain, it cannot be calculated from first principles. Therefore, only phenomenological, typically Gribov–Regge theory inspired, predictions can be compared to the experimental data. Analyticity and unitarity lead to the Froissart–Martin bound [13] which limits the total cross-section dependence on the centre-of-mass energy to $\ln^2 s$.

The cross-section measurement is a counting experiment. The cross-section value is calculated as the ratio of the number of signal events to the integrated luminosity and it is corrected for the trigger and tracking inefficiencies. Typically, in the collider experiments, the fiducial cross section is measured and later, using the estimation of the acceptance, its value is extrapolated to the full phase space. Such a procedure was also applied by ATLAS — see [14] for details. The data used in the presented analysis were selected using the MBTS system and the sample corresponds to the integrated luminosity of 63 ± 6 pb^{-1}. The mean number of the pp collisions per bunch crossing was about 0.002.

Inelastic proton–proton interactions can be divided into two classes. Non-diffractive interactions are mediated by an exchange of a colour octet, while the diffractive ones are due to the exchange of a colour singlet. In the interaction, at least one proton dissociates and the larger of the two dissociation system masses, M_X, is used to determine the fiducial region. The MBTS system efficiency is larger than 50% for $\tilde{\xi} = \tilde{M}_X^2/s > 10^{-6}$ (tilde denotes the hadron level quantities), which defines the fiducial region of the inelastic pp cross-section measurement.

The inelastic fiducial cross section can be calculated as

$$\sigma_{\rm inel}\left(\tilde{\xi} > 10^{-6}\right) = \frac{N - N_{\rm bg}}{\epsilon_{\rm trig}\, L}\, \frac{1 - f_{\tilde{\xi}<10^{-6}}}{\epsilon_{\rm sel}}\,, \tag{1}$$

where N is the number of events passing the selection, $N_{\rm bg}$ is the number of background events, $\epsilon_{\rm trig}$ is the trigger efficiency, L denotes the integrated luminosity, $1 - f_{\tilde{\xi}<10^{-6}}$ accounts for migrations of events with $\tilde{\xi} < 10^{-6}$ into the fiducial region, and $\epsilon_{\rm sel}$ is the event off-line selection efficiency. The first term in Eq. (1) was determined from the data, while the second using the Monte Carlo. An important ingredient of the analysis was the fraction of the cross sections for single (SD) and double (DD) diffractive interactions to the inelastic ones, $f_{\rm D} = (\sigma_{\rm SD} + \sigma_{\rm DD})/\sigma_{\rm inel}$. This fraction was estimated from the data in the model-dependent way by comparing the rates of independent triggers and predictions of various Monte Carlo models. The measured fiducial cross section at $\sqrt{3} = 13$ TeV is

$$\sigma_{\rm inel}\left(\tilde{\xi} > 10^{-6}\right) = [65.2 \pm 0.8({\rm exp.}) \pm 5.9({\rm lumi.})]\ {\rm mb}\,.$$

The fiducial cross section, $\sigma_{\rm inel}(\tilde{\xi} > 10^{-6})$, was extrapolated to the full phase space. The extrapolation was performed with the help of PYTHIA 8 MC using the Donnachie–Landshoff model [15] with the Pomeron trajectory $\alpha(t) = 1 + \epsilon + \alpha'\, t$, $\epsilon = 0.085$ and $\alpha' = 0.25$ GeV^{-2}. The estimation of the detector acceptance was carried out using various Monte Carlo models. The range of the acceptance variation was taken as the extrapolation uncertainty. The extrapolated cross section

$$\sigma_{\rm inel} = [73.1 \pm 0.9({\rm exp.}) \pm 6.6({\rm lumi.}) \pm 3.8({\rm extr.})]\ {\rm mb}$$

is compared to other measurements [16–18] in Fig. 7. The experimental data presented in this figure are also compared to the predictions of PYTHIA, EPOS LHC and QGSJET-II and of the models by Block and Halzen [19] and by Achilli *et al.* [20].

The value obtained at $\sqrt{s} = 13$ TeV matches well the other measurements. The energy dependence of the inelastic proton–proton cross section is well-described by the Monte Carlo and Regge–Gribov motivated models.

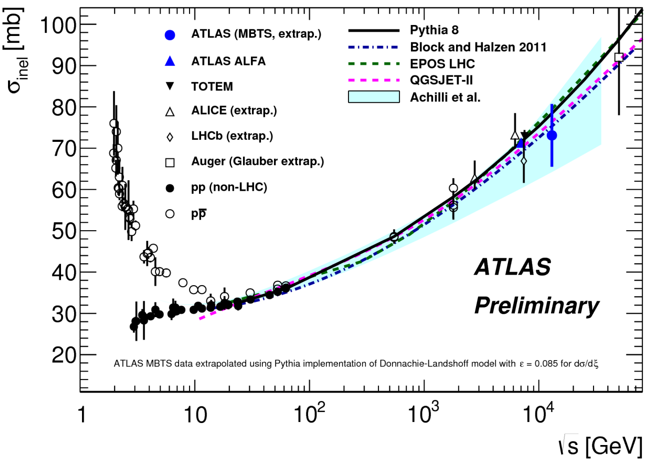

Fig. 7. The inelastic cross section *vs.* $\sqrt{s}$. The ATLAS results and other measurements [16–18] are also shown. The data are compared to the predictions of PYTHIA, EPOS LHC and QGSJET-II MC and of the models by Block and Halzen [19] and by Achilli *et al.* [20]. From [14].

5. Selected final states

In the following, the production cross sections of selected final states in proton–proton interactions are discussed.

5.1. Inclusive jet cross section

The analysis of jet properties is a tool to test perturbative QCD (pQCD) at the TeV energy scale. The jets are results of the fragmentation and a subsequent hadronisation of the quarks and gluons produced in a hard process. The production cross sections of high transverse momentum jets can be calculated within the perturbative QCD.

The ATLAS Collaboration performed such an analysis [21] using 78 pb^{-1} of data. The data had to pass quality requirements. The jets were identified using the anti-k_t algorithm [22] assuming the jet radius parameter of $R = 0.4$. The reconstructed jets were required to belong to the central rapidity[2] interval defined by $|y| < 0.5$. The data were corrected for the experimental effects and unfolded.

Figure 8 shows the distribution of the jet transverse momentum. Predictions of the NLO perturbative QCD carried out using NLoJet++ [23] are

---

[2] The jet rapidity is defined as $y = \frac{1}{2}\ln\frac{E+p_z}{E-p_z}$, where E and p_z are the jet energy and longitudinal momentum, respectively.

also presented. The pQCD predictions were obtained using the CT10 parton distribution function (PDF) [24] and were corrected for non-pertubative effects.

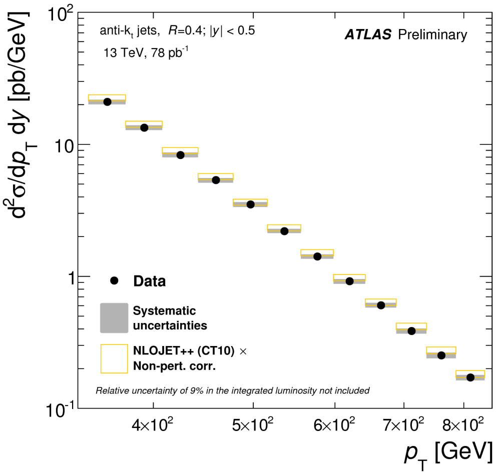

Fig. 8. Inclusive-jet cross sections as a function of the jet p_T in $|y| < 0.5$, for anti-k_t jets with $R = 0.4$. NLO pQCD predictions calculated using NLoJet++ with the CT10 NLO PDF set are also shown. From [21].

The measured cross sections vary by two orders of magnitude. They are well-described by the perturbative QCD calculations. The ratio of the measured cross sections to the predictions are presented in Fig. 9. Predictions

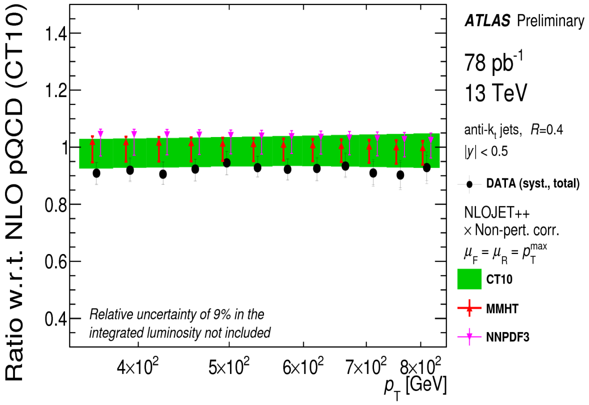

Fig. 9. Ratio of the measured inclusive-jet cross section to the NLO pQCD prediction (NLoJet++ with CT10 PDF), as a function of the jet p_T in $|y| < 0.5$, for anti-k_t jets with $R = 0.4$. From [21].

calculated using the MMHT [25] and the NNPDF3.0 [26] NLO parton density distribution sets are also shown in the figure. Within the uncertainties, the data and the predictions are in a good agreement.

5.2. Inclusive W/Z production

Measurements of the production of electroweak gauge bosons provide additional tests of our understanding of pQCD and electroweak processes. These bosons are produced with relatively large cross sections and can be identified via their decays into leptons. The theoretical predictions, accurate up to the next-to-next-to-leading-order (NNLO), are available and they include NLO electroweak corrections. Since the cross-section predictions depend on the parton distribution functions, they are sensitive to the underlying dynamics of the strongly interacting protons.

The measurement of the $W^{\pm}$ and Z production cross sections was performed by ATLAS [27] at $\sqrt{s} = 13$ TeV using approximately 85 pb^{-1} of the data collected in July 2015. The bosons were identified by their leptonic decays $W^{\pm} \to l^{\pm}\mu$, $Z \to l^{+}l^{-}$, where $l = e, \mu$.

The fiducial region of the $W^{\pm}$ measurement was defined imposing the following requirements: (a) the transverse momentum of the lepton $p_{\mathrm{T}}^{l} >$ 25 GeV; (b) the missing transverse energy, $E_{\mathrm{T}}^{\mathrm{miss}} > 25$ GeV (in the case of Monte Carlo, the neutrino transverse momentum $p_{\mathrm{T}}^{\nu} > 25$ GeV); (c) the lepton pseudorapidity $|\eta_{\mathrm{l}}| < 2.5$; (d) the transverse mass

$$m_{\mathrm{T}} = \sqrt{2p_{\mathrm{T}}^{l}p_{\mathrm{T}}^{\nu}[1 - \cos(\phi_l - \phi_\nu)]} > 50\ \mathrm{GeV}\,,$$

where $\phi_l(\phi_\nu)$ is the azimuthal angle of the lepton (missing mass, neutrino). To measure the Z production fiducial cross section the region was defined as: (a) $p_{\mathrm{T}}^{l} > 25$ GeV; (b) $|\eta_l| < 2.5$; (c) the dilepton effective mass, $66 < m_{ll} <$ 116 GeV.

The experimental data were corrected for the inefficiencies of the event selection, reconstruction and lepton identification as well as for the trigger efficiency. These corrections were estimated either directly from the data or using the Monte Carlo generated samples — see also [27].

Background contributions due to the single and diboson production as well as to that of the top quark were estimated using Monte Carlo generators. Nearly all expected contributions were generated using POWHEG-BOX2 [28] interfaced to PYTHIA 8. The programs used CT10 PDF set and the AZNLO CTEQL1 tune [29]. The EvtGen 1.2.0 [30] was used for properties of the bottom and charm hadron decays, and PHOTOS++ 3.52 [31] was used for QED emissions from electroweak vertices and charged leptons. Samples of top quark pairs were generated with POWHEG-BOX2 and those due to diboson production with Sherpa 2.1.1 [32] with the matrix elements containing the resonant WW, WZ and ZZ processes. All other diagrams with four electroweak vertices were also included in the calculations. Multijet events were simulated with PYTHIA 8 and using EvtGen 1.2.0 for correct simulation of the bottom and charm hadron decays. Table II lists the expected fractions of events in each considered channel.

TABLE II

Expected fractions (in %) of events in the considered channels.

Channel	$W \to e\nu$	$W \to \mu\nu$	$Z \to e^+e^-$	$Z \to \mu^+\mu^-$
$W \to \tau\nu$	1.8	2.0	—	—
$Z \to \tau\tau$	0.2	0.2	< 0.1	< 0.1
Diboson	—	—	0.1	0.1
$t\bar{t}$	1.2	1.1	0.5	0.5
$W \to e\nu$	95.6	—	< 0.1	—
$W \to \mu\nu$	—	92.0	—	< 0.1
$Z \to e^+e^-$	1.2	—	99.4	—
$Z \to \mu^+\mu^-$	—	4.7	—	99.4

The measured transverse mass, m_{T}, and the dilepton mass, $m_{\mu\mu}$, are shown in Fig. 10 for the $W \to e\nu$ and $Z \to \mu^+\mu^-$ samples. The discussed above background contributions are also presented in the figure. The data are well-described by Monte Carlo predictions.

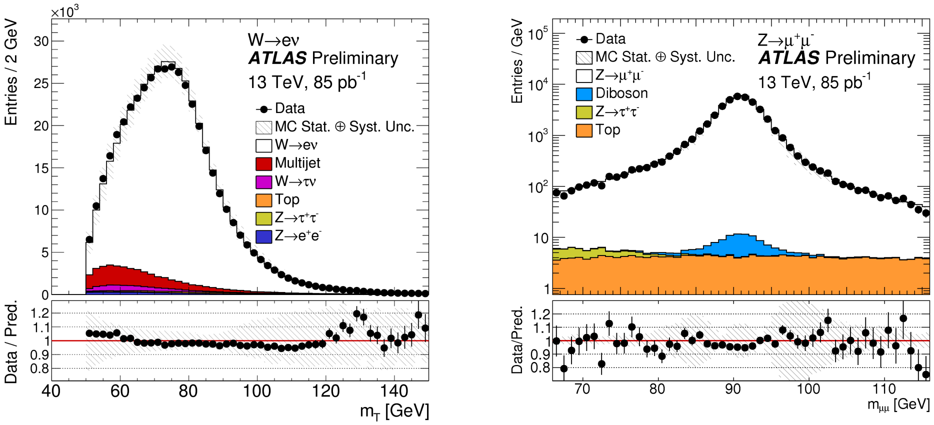

Fig. 10. Left: the measured transverse mass distribution, m_{T} for the $W \to e\nu$ sample. Right: the measured dilepton mass distribution, $m_{\mu\mu}$ for $Z \to \mu^+\mu^-$ channel. Contributions of particular background processes are marked. From [27].

The obtained fiducial cross sections for the W and Z production are depicted in Fig. 11 together with results of the calculations using various parton distribution functions of the proton. The fiducial cross sections are free from theoretical uncertainties on the acceptance. The largest contribution to the total uncertainty comes from the luminosity measurement which gives 9% alone. The data and the NNLO level calculations are in a good agreement.

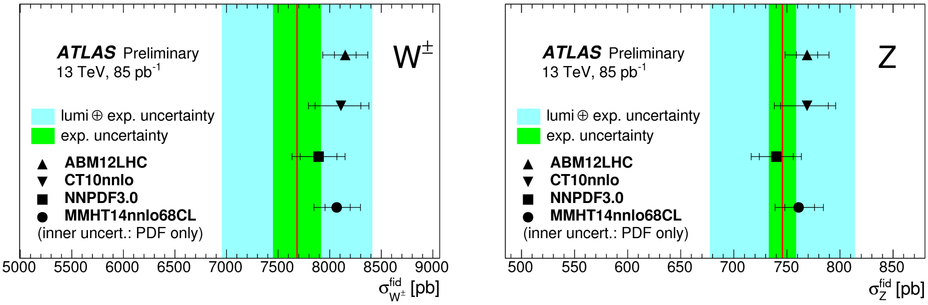

Fig. 11. Left: the fiducial cross section for W production, $\sigma^{\mathrm{fid}}_{W\pm}$. Right: the fiducial cross section for Z production, $\sigma^{\mathrm{fid}}_{Z}$. The NNLO level calculations using various PDF sets are also depicted. From [27].

To get rid of the luminosity uncertainty the ratios of the fiducial cross sections were calculated. The results are presented in Fig. 12 with predictions of the calculations using the NNLO PDF sets. The predictions are in a fair agreement with the experimental data. The predicted values of $\sigma^{\mathrm{fid}}_{W+}/\sigma^{\mathrm{fid}}_{W-}$ calculated with different PDF versions are scattered in a manner comparable to the experimental uncertainties. The predicted values of $\sigma^{\mathrm{fid}}_{W\pm}/\sigma^{\mathrm{fid}}_{Z}$ (Fig. 12 (right)) agree within the quoted uncertainties and are consistent with the measured ratio of the cross sections.

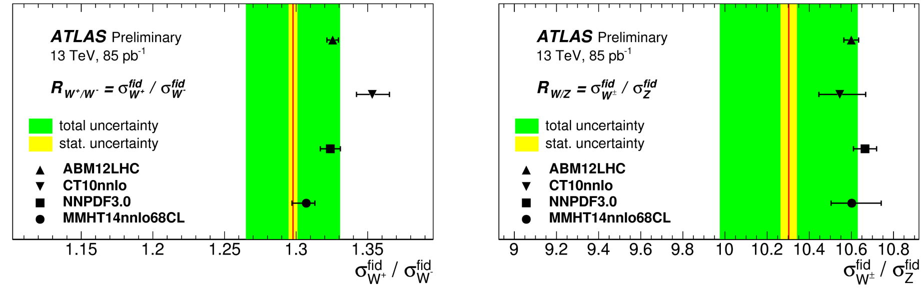

Fig. 12. Ratio of the fiducial cross sections $\sigma^{\mathrm{fid}}_{W+}/\sigma^{\mathrm{fid}}_{W-}$ (left), ratio of the fiducial cross sections $\sigma^{\mathrm{fid}}_{W\pm}/\sigma^{\mathrm{fid}}_{Z}$ (right). The NNLO level calculations using various PDF sets are also shown. From [27].

The total inclusive $W^{\pm}$ production cross sections times the single lepton-flavour branching ratio are:

$$\sigma^{\mathrm{tot}}{}_{W^+} = [10960 \pm 20(\mathrm{stat.}) \pm 440(\mathrm{syst.}) \pm 990(\mathrm{lumi.})]\ \mathrm{pb}$$

and

$$\sigma^{\mathrm{tot}}{}_{W^-} = [8380 \pm 20(\mathrm{stat.}) \pm 350(\mathrm{syst.}) \pm 750(\mathrm{lumi.})]\ \mathrm{pb}$$

for W^+ and W^-, respectively. The total inclusive Z boson production cross section times leptonic branching ratio, within the invariant mass window of the lepton pair $66 < m_{ll} < 116$ GeV, is

$$\sigma^{\mathrm{tot}}{}_{Z} = [1869 \pm 7(\mathrm{stat.}) \pm 42(\mathrm{syst.}) \pm 168(\mathrm{lumi.})]\ \mathrm{pb}\,.$$

The total inclusive cross section times the branching ratio to the leptonic channels as a function of the centre-of-mass energy is presented in Fig. 13. Left panel shows the energy dependence of $\sigma_W \times \mathrm{Br}(W \to l\nu)$ and the right one that of $\sigma_{Z/\gamma^\star} \times \mathrm{Br}(Z/\gamma^\star \to l^+l^-)$. The data measured by other experiments at different colliders and at lower values of $\sqrt{s}$ are also shown. Also, the predictions calculated using the MSTW2008 NNLO [4] PDF set are depicted in the figure.

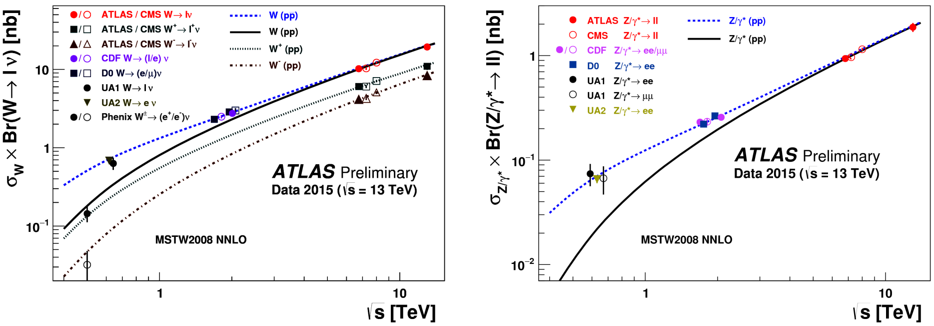

Fig. 13. Left: the energy dependence of $\sigma_W \times \mathrm{Br}(W \to l\nu)$. Right: the energy dependence of $\sigma_{Z/\gamma^\star} \times \mathrm{Br}(Z/\gamma^\star \to l^+l^-)$. Data measured at lower values of $\sqrt{s}$ and other experiments are also shown. NNLO pQCD predictions calculated with MSTW2008 NNLO PDF set are depicted. From [27].

The cross sections measured at 13 TeV follows the energy dependence already seen at lower values of $\sqrt{s}$. The experimental data are well-described by the NNLO perturbative QCD calculations.

5.3. *Cross section for Z+jets production*

Investigation of the production of the Z boson associated with jets provides yet another tool to test the Standard Model. In the analysis [33], the

Z boson was identified using its decay to e^+e^- or $\mu^+\mu^-$ pair. The leptons had to pass the selection criteria imposing the reconstruction and isolation quality conditions. They were requested to have the transverse momentum $p_{\mathrm{T}}^l > 25$ GeV and the pseudorapidity $|\eta^l| < 2.5$. The considered dilepton effective mass range was $66 < m_{ll} < 116$ GeV. Hadron jets were reconstructed with the anti-k_{t} algorithm with $R = 0.4$. They were required to have the transverse momentum of at least 30 GeV and the rapidity $|y| < 2.5$ and to pass the pileup reduction criteria. A jet closer in the (η, ϕ) plane than 0.4 to the selected lepton was discarded. The event categories were defined using the minimum number of jets accompanying the Z boson. The data sample corresponds to the integrated luminosity of 85 pb^{-1} collected in July 2015.

Monte Carlo simulations were normalised to the results of the highest order calculations available and were used to compare the data and Z + jets production predictions and to estimate the contribution of backgrounds. Signal events were simulated using Sherpa 2.1.1. Matrix elements were calculated for up to two partons at NLO and up to four additional partons at LO using the Comix [34] and OpenLoops [35] matrix element generators and subsequently merged with the Sherpa parton shower [36] using the ME+PS@NLO prescription [37]. Additionally, MadGraph5_aMC@NLO 2.2.2 [38] was used to simulate events of Z + jets production. Explicit matrix elements for up to four partons at the leading order were used. Background processes were generated in the same manner as for the analysis of the inclusive $W^\pm$ and Z production [27].

Figure 14 (left) presents the combined fiducial cross sections for $Z \to l^+l^-$ plus $\geq N_{\mathrm{jets}}$ as a function of the multiplicity of associated jets, N_{jets}. The cross-section ratios for successive jet multiplicities are shown in Fig. 14 (right). The uncertainty on the measurements ranges from 10% to 20%. The experimental data are reasonably well-described by the predictions calculated with Sherpa and MadGraph. Table III lists the combined fiducial cross sections for production of $Z \to l^+l^-$ plus $\geq N_{\mathrm{jets}}$ reported at the Born level together with statistical, systematic and luminosity uncertainties.

TABLE III

Combined fiducial cross sections for $Z \to l^+l^-$ plus $\geq N_{\mathrm{jets}}$ reported at the Born level together with statistical, systematic and luminosity uncertainties.

$\mathrm{N_{jets}}$ limit	σ	± stat. [pb]	± syst.	± lumi.
≥ 1	115.7	1.3	4.9	10.4
≥ 2	27.0	0.6	1.4	2.4
≥ 3	5.8	0.3	0.4	0.5
≥ 4	1.40	0.14	0.11	0.13

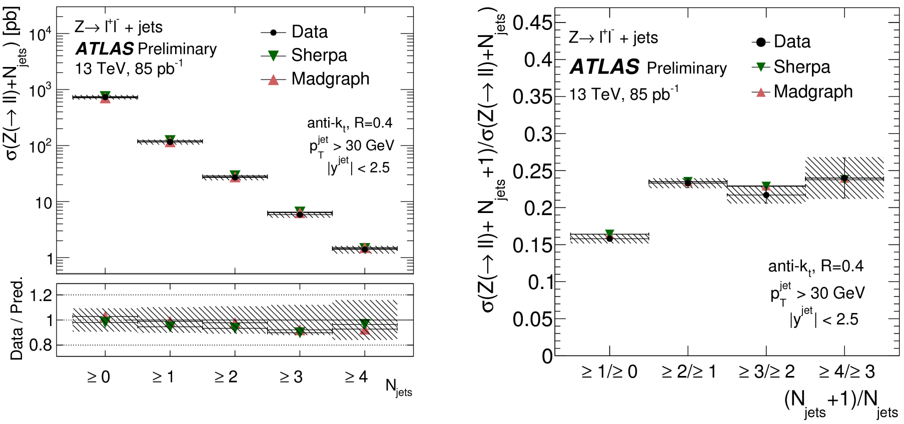

Fig. 14. Combined $Z \to l^+l^-$ plus $\geq N$ jets fiducial cross sections (left), and cross-section ratios for successive jet multiplicities (right). Results are reported at the Born level and compared to predictions of Sherpa and MadGraph. The hatched error band corresponds to the total uncertainty of the results: systematic, statistical, and luminosity uncertainties. From [33].

5.4. Inclusive isolated photon production

Analysis of the prompt photon production in proton–proton interactions provides the pQCD test-bed in the environment which is less affected by the hadronisation effects than the jet production. There are two leading order pQCD processes contributing to prompt photon production. The direct-photon production in which a photon is produced in a hard process and the fragmentation-photon production in which a photon is radiated in the fragmentation of a parton produced with a large p_{T}. Measurements of isolated photons are very difficult from the experimental point of view. They required a careful experimental analysis which also yielded both the definition of the isolation criteria and the determination of backgrounds using the data. Here, it was important to properly estimate and reject the decay products of neutral hadrons. Such an analysis was performed by ATLAS using 6.4 ± 0.6 pb^{-1} of data taken at $\sqrt{s} = 13$ TeV in 2015 — see [39] for details. The photons were required to have the transverse energy $E_{\mathrm{T}}^{\gamma} > 120$ GeV, the pseudorapidity $|\eta^{\gamma}| < 2.37$ and to pass the isolation criteria. In this kinematic domain, the trigger was highly efficient. The analysis excluded the barrel — end-cap transition region $(1.37 < |\eta^{\gamma}| < 1.56)$. The main contribution to the background are the multi-jet events with a jet misidentified as a photon. Such a jet typically contains a very energetic π^0 decaying into two collimated photons. Measurements of the isolated photon were performed at $\sqrt{s} = 7$ TeV by ATLAS [40] and CMS [41].

Figure 15 presents the distribution of the photon transverse energy, E_{T}^{γ}, for events passing the selection criteria. The Sherpa 2.1.1 predictions obtained using with NLO CT10 PDF were normalised to the total yield observed in the data. The measured distribution is well-described by the Monte Carlo predictions.

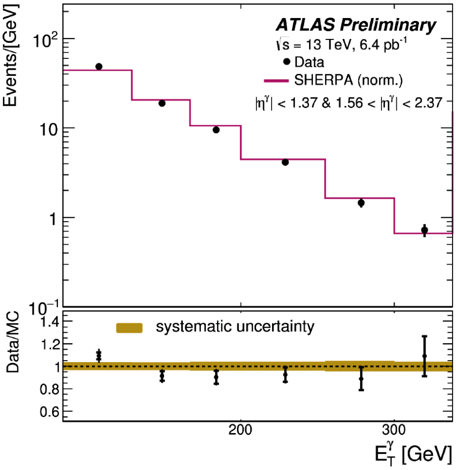

Fig. 15. The distribution of the isolated photon transverse energy for $|\eta^{\gamma}| < 2.37$ excluding region of $1.37 < |\eta^{\gamma}| < 1.56$. The Sherpa 2.1. predictions normalised to the measured signal yield are also shown. From [39].

6. Summary

Thanks to the machine crew, the LHC is operational after the Long Shutdown 1. The machine smoothly passed few improvements and delivers high intensity proton beams accelerated to 6 500 GeV. A large centre-of-mass energy range, from 900 GeV to 13 TeV, is now accessible for the LHC experiments.

Selected Standard Model results obtained with the ATLAS detector during the early phase of the LHC Run 2 were presented. The measurements carried out at $\sqrt{s} = 13$ TeV follow the energy dependences already observed at lower energies. A reasonable agreement of theoretical predictions with data is observed. The Monte Carlo models tuned using lower energy data provide a reasonable description of 13 TeV data. The extrapolated value of the inelastic cross section is $\sigma_{\mathrm{inel}} = [73.1 \pm 0.9(\mathrm{exp.}) \pm 6.6(\mathrm{lumi.}) \pm 3.8(\mathrm{extr.})]$ mb. Preliminary results on the gauge boson production already show a discriminating power towards various parton distribution functions. The total inclusive $W^{\pm}$ production cross sections times the single lepton-flavour branching ratios are: $\sigma^{\rm tot}_{W+} = [10960 \pm 20(\text{stat.}) \pm 440(\text{syst.}) \pm 990(\text{lumi.})]$ pb and $\sigma^{\rm tot}_{W+} = [8380 \pm 20(\text{stat.}) \pm 350(\text{syst.}) \pm 750(\text{lumi.})]$ pb for W^+ and W^-, respectively. The total inclusive Z boson production cross section times leptonic branching ratio, within the dilepton pair invariant mass window $66 < m_{ll} < 116$ GeV, is ${\sigma^{\rm tot}}_Z = [1869 \pm 7(\text{stat.}) \pm 42(\text{syst.}) \pm 168(\text{lumi.})]$ pb.

I am very indebted to Prof. Anna Kaczmarska and Dr. Rafał Staszewski for many discussions. This work is supported in part by the Polish National Science Centre grant UMO-2012/05/B/ST2/02480.

REFERENCES

[1] ATLAS Collaboration, *JINST* **3**, S08003 (2008).

[2] ATLAS Collaboration, `arXiv:1602.01633 [hep-ex]`.

[3] T. Sjöstrand, S. Mrenna, P. Skands, *Comput. Phys. Commun.* **178**, 852 (2008); *J. High Energy Phys.* **0605**, 026 (2006).

[4] A. Martin, W. Stirling, R. Thorne, G. Watt, *Eur. Phys. J. C* **63**, 189 (2009).

[5] ATLAS Collaboration, ATLAS Note ATL-PHYS-PUB-2011-014, 2011, `http://cds.cern.ch/record/1400677`

[6] S. Carrazza, S. Forte, J. Rojo, `arXiv:1311.5887 [hep-ph]`.

[7] P. Skands, S. Carrazza, J. Rojo, *Eur. Phys. J. C* **74**, 3024 (2014).

[8] T. Pierog *et al.*, *Phys. Rev. C* **92**, 034906 (2015).

[9] S. Ostapchenko, *Phys. Rev. D* **83**, 014018 (2011).

[10] ATLAS Collaboration, ATLAS Note ATL-PHYS-PUB-2015-019, CERN Geneva, July 2015, `http://cds.cern.ch/record/2037684`

[11] ATLAS Collaboration, Tech. Rep. ATL-PHYS-PUB-2014-021, 2014, `https://cds.cern.ch/record/1966419`

[12] M. Bahr *et al.*, *Eur. Phys. J. C* **58**, 639 (2008).

[13] M. Froissart, *Phys. Rev.* **123**, 1053 (1961); A. Martin, *Nuovo Cim. A* **42**, 930 (1965).

[14] ATLAS Collaboration, ATLAS Note ATL-CONF-2015-038, CERN, Geneva, August 2015, `http://cds.cern.ch/record/2045064`

[15] A. Donnachie, P. Landshoff, *Nucl. Phys. B* **244**, 322 (1984).

[16] K.A. Olive *et al.* [Particle Data Group], *Chin. Phys. C* **38**, 090001| (2014).

[17] G. Antchev *et al.* [TOTEM Collaboration], *Europhys. Lett.* **101**, 21004 (2013); B. Abelev *et al.* [ALICE Collaboration], *Eur. Phys. J. C* **73**, 2456 (2013); R. Aaij *et al.* [LHCb Collaboration], *J. High Energy Phys.* **1502**, 129 (2015).

[18] P. Abreu *et al.* [Pierre Auger Collaboration], *Phys. Rev. Lett.* **109**, 062002 (2012).

[19] M.M. Block, F. Halzen, *Phys. Rev. D* **83**, 077901 (2011).

[20] A. Achilli *et al.*, *Phys. Rev. D* **84**, 094009 (2011).

[21] ATLAS Collaboration, ATLAS Note ATL-CONF-2015-034, CERN, Geneva, July 2015, `http://cds.cern.ch/record/2038145`

[22] M. Cacciari, G.P. Salam, G. Soyez, *J. High Energy Phys.* **0804**, 063 (2008); *Eur. Phys. J. C* **72**, 1896 (2012).

[23] Z. Nagy, *Phys. Rev. D* **68**, 094002 (2003).

[24] H.-L. Lai *et al.*, *Phys. Rev. D* **82**, 074024 (2010).

[25] L.A. Harland-Lang, A.D. Martin, P. Motylinski, R.S. Thorne, *Eur. Phys. J. C* **75**, 204 (2015).

[26] R.D. Ball *et al.*, *J. High Energy Phys.* **1504**, 040 (2015).

[27] ATLAS Collaboration, ATLAS Note ATL-CONF-2015-039, CERN, Geneva, August 2015, `http://cds.cern.ch/record/2045487`

[28] P. Nason, *J. High Energy Phys.* **0411**, 040 (2004); S. Frixione, P. Nason, C. Oleari, *J. High Energy Phys.* **0711**, 070 (2007); S. Alioli, P. Nason, C. Oleari, E. Re, *J. High Energy Phys.* **1006**, 043 (2010); **0807**, 060 (2008).

[29] ATLAS Collaboration, *J. High Energy Phys.* **1409**, 145 (2014).

[30] D.J. Lange, *Nucl. Instrum. Methods Phys. Res. A* **462**, 152 (2001).

[31] N. Davidson, T. Przedzinski, Z. Was, *Comput. Phys. Commun.* **199**, 86 (2016).

[32] T. Gleisberg *et al.*, *J. High Energy Phys.* **0902**, 007 (2009).

[33] ATLAS Collaboration, ATLAS Note ATL-CONF-2015-041, CERN, Geneva, August 2015, `http://cds.cern.ch/record/2048104`

[34] T. Gleisberg, S. Höche, *J. High Energy Phys.* **0812**, 039 (2008).

[35] F. Cascioli, P. Maierhofer, S. Pozzorini, *Phys. Rev. Lett.* **108**, 111601 (2012).

[36] S. Schumann, F. Krauss, *J. High Energy Phys.* **0803**, 038 (2008).

[37] S. Höche, F. Krauss, M. Schönherr, F. Siegert, *J. High Energy Phys.* **1304**, 027 (2013).

[38] J. Alwall *et al.*, *J. High Energy Phys.* **1407**, 079 (2014).

[39] ATLAS Collaboration, ATLAS Note ATL-PHYS-PUB-2015-016, CERN, Geneva, July 2015, `http://cds.cern.ch/record/2037667`

[40] ATLAS Collaboration, *Phys. Rev. D* **89**, 052004 (2014); *Phys. Lett. B* **706**, 150 (2011).

[41] CMS Collaboration, *Phys. Rev. Lett.* **106**, 082001 (2011); *Phys. Rev. D* **84**, 052011 (2011).